

Volume 4 [Full Papers], Pages 62–78 ISSN: 2753-8168

Implementation of a VoF solver with phase change for the simulation of internal cavitation and droplet breakup in injectors

Bjørn Christian Dueholm^{1,*}, Jesper de Claville Christiansen¹, Benny Endelt¹, Nikolaj Kristensen², and Jakob Hærvig³

¹Department of Materials and Production, Aalborg University, Pontoppidanstræde 103, 9220 Aalborg East, Denmark

²Hans Jensen Lubricators A/S, Smedevænget 3, 9560 Hadsund, Denmark

 3 Department of Energy, Aalborg University, Pontoppidanstræde 111, 9220 Aalborg East, Denmark $Email\ address\colon \texttt{bcd@mp.aau.dk}$

DOI: https://doi.org/10.51560/ofj.v4.111

Results with version(s): OpenFOAM® v9 and v2106

Repository: https://github.com/BCDueholm/inter3PhaseChangeFoam

Abstract. This study presents the implementation and derivation of a Volume of Fluid (VoF) solver capable of considering pressure-driven phase change and handling three fluids. The implemented code is designed to investigate internal nozzle cavitation and subsequent injection and jet breakup. An extended cavitation model is also implemented to handle phase change in the presence of a third phase. Detailed descriptions and derivation of the mathematical system are presented. The solver is verified on a one-dimensional benchmark case from the literature and validated on an experimentally well-documented geometry. The validation shows the developing cavitation regime is well captured by comparing velocity profiles and flow images with experimental measurements and visualisation.

1. Introduction

The phenomenon of cavitation in injectors and the subsequent breakup of liquid droplets play pivotal roles in a wide range of engineering applications, including fuel injection systems, sprays and atomisers. Understanding and accurately modelling cavitation and droplet breakup are paramount for optimising combustion processes, improving fuel efficiency, reducing emissions and enhancing overall performance in various industries. The field of research is active and ongoing. Several authors have recently studied cavitation, especially in fuel nozzles [1–5]. Cavitation is characterised by the formation, growth and collapse of gas bubbles within a liquid caused by a low static pressure. The low static pressure can be flow-induced, but it can also be created by other means, such as vibration. In the context of injectors, high-pressure gradients induce flow separation around geometric obstacles. The flow separation causes the local static pressure to fall low enough for vapour to be formed [6] or for small entrained gas bubbles to grow in size. When cavitation in injectors is studied, it is often of interest to determine how the cavitation affects the droplet size and what the droplet size distribution becomes further downstream. There are generally two approaches to determining cavitation's influence on the breakup by simulation. The first approach uses primary and secondary breakup models to model the breakup of droplets using the Lagrangian framework. The internal nozzle dynamics would then typically be simulated using an Euler-Euler approach, and some form of coupling model would be implemented to go from internal nozzle flow to the Lagrangian phase. Ravendran used a method like this [7], where the internal nozzle dynamics were simulated using a Homogeneous Mixture Model (HEM) and a coupling method was used to transfer the internal flow characteristics into a Lagrangian framework. In the Lagrangian framework, primary and secondary breakup models were used to model the rest of the spray formation. The second approach is to simulate the entire breakup using an Euler-Euler approach or simulate most of the primary breakup using an Euler-Euler

Received: 11 July 2023, Accepted: 22 February 2024, Published: 8 April 2024

^{*} Corresponding author

approach and then coupling to a Lagrangian model. Generally, the latter approach is used as it saves computational resources. Heinrich and Schwarze [8] simulated the primary breakup using a Volume of Fluid (VoF) model and moved the droplets formed from the primary breakup into a Lagrangian framework using a sphericity criterion. Their results showed good agreement with experimental measurements; however, there was no cavitation inside the injector. The current study follows the second approach. It implements an extension of the OpenFOAM solver for cavitating flows called interPhaseChangeFoam. interPhaseChangeFoam is a solver for two fluids, extended here to take a third non-condensing fluid into account. This is done by implementing functionality from the solver interMixingFoam and making the necessary changes to accommodate an extra fluid in interPhaseChangeFoam. A new cavitation model is also derived and implemented. The cavitation model was first described by Yuan and Schnerr [9]. It can include the interaction of external gas on the liquid and vapour flowing through the nozzle. The external gas can interact with the cavitation regime if the vapour extends all the way to the exit of the nozzle. Pressure waves from collapsing vapour pockets can also travel out the nozzle exit and interact in the spray breakup. The implementation of the cavitation model from [9] in OpenFOAM was first done by [10]. The implementation presented in this paper is based on their work. It, however, uses a different approach to solving the system of volume fraction equations to ensure mass conservation and does not model artificial interface compression or diffusion between the gas phases. This paper presents the mathematics behind the implementation in great detail and publishes the code alongside it to increase the usability of the work. The implementation is done to investigate injector nozzles. In injector nozzles, there is often cavitation inside the nozzle and air outside. To investigate the influence of cavitation on how a spray is formed, it is necessary to consider all three fluids.

2. Theoretical backgroud

The theoretical background in terms of governing equations, cavitation model and the mathematical system has been described by the author in previous work [11], as part of a PhD course. It is included in this paper for completeness and to aid the reader. The Volume of Fluid (VoF) method is an Euler-Euler approach where one set of momentum and continuity equations are solved using the effective fluid properties. It is assumed that each fluid is incompressible and isothermal. Transport equations are solved to track each fluid together with the momentum and continuity equation. The variable α is used for each volume fraction. It is defined as

$$\alpha_i = \frac{V_i}{V}.\tag{1}$$

Here V is the volume of each cell, and i denotes the $i^{\rm th}$ fluid. α is used to track different fluids as they are solved as one mixture. The volume fractions are summed up to unity as

$$\sum_{i=1}^{3} \alpha_i = 1. \tag{2}$$

Having three fluids, l,v and nc are used as the subscripts to represent liquid, vapour and non-condensing gas, respectively. The properties of the mixture are also blended between the fluids as

$$\rho = \sum_{i=1} \alpha_i \rho_i, \qquad \mu = \sum_{i=1} \alpha_i \mu_i, \qquad (3)$$

where ρ is the density and μ is the dynamic viscosity.

2.1. Governing equations. The continuity and momentum equations are given as

$$\nabla \cdot \mathbf{U} = -\frac{1}{\rho} \frac{d\rho}{dt},\tag{4}$$

$$\nabla \cdot \mathbf{U} = -\frac{1}{\rho} \frac{d\rho}{dt},$$

$$\frac{\partial (\rho \mathbf{U})}{\partial t} + \nabla \cdot (\rho \mathbf{U} \otimes \mathbf{U}) = -\nabla \hat{p} + \nabla \cdot \boldsymbol{\tau} + \mathbf{f}_{\sigma} - \mathbf{g} \cdot \mathbf{h} \nabla \rho,$$
(5)

respectively. Here \hat{p} is modified pressure, which is constructed by removing the hydrostatic pressure from the static pressure p. τ is the deviatoric stress tensor, f_{σ} is the surface tension force, g is the acceleration of gravity, **U** is the velocity vector, t is time and $\mathbf{g} \cdot \mathbf{h} \nabla \rho$ is a term added as a consequence of using \hat{p} , where \mathbf{h} is the position vector.

The transport equation of the volume fraction of each phase is given by

$$\frac{\partial \alpha_{l}}{\partial t} + \nabla \cdot (\alpha_{l} \mathbf{U}) = -\frac{\dot{m}}{\rho_{l}},\tag{6}$$

$$\frac{\partial \alpha_{\mathbf{v}}}{\partial t} + \nabla \cdot (\alpha_{\mathbf{v}} \mathbf{U}) = \frac{\dot{m}}{\rho_{\mathbf{v}}},\tag{7}$$

$$\frac{\partial \alpha_{\rm nc}}{\partial t} + \nabla \cdot (\alpha_{\rm nc} \mathbf{U}) = 0. \tag{8}$$

Here \dot{m} is the mass transfer rate between $\alpha_{\rm l}$ and $\alpha_{\rm v}$. The mass transfer term is calculated in OpenFOAM by a cavitation model. As seen from Eqn. 7 and Eqn. 8 the model does not contain any diffusion between the gas phases in the system. This assumption is considered valid for injectors with cavitation, as the two gas phases are generally separated from each other. This, however, also limits the applicability of the implementation in cases where the two gas phases interact. Because mass is transferred between the two phases, the divergence of velocity is no longer zero. Eqn. 6 to Eqn. 8 can be rewritten to the form shown in Eqn. 9, here exemplified with $\alpha_{\rm l}$ as

$$\frac{d\alpha_{l}}{dt} + \alpha_{l}\nabla \cdot (\mathbf{U}) = -\frac{\dot{m}}{\rho_{l}},\tag{9}$$

by using the definition of the total derivative and the product rule for divergence. For more details on this, refer to Appendix A. In Eqn. 9, d denotes the total derivative, which is used throughout this paper. By adding Eqn. 6 to Eqn. 8 on the rewritten form, it can be shown that the divergence of velocity is different from zero as

$$\frac{d}{dt}\left(\alpha_{l} + \alpha_{v} + \alpha_{nc}\right) + \left(\alpha_{l} + \alpha_{v} + \alpha_{nc}\right) \nabla \cdot \mathbf{U} = \left(-\frac{1}{\rho_{l}} + \frac{1}{\rho_{v}}\right) \dot{m},\tag{10}$$

$$\nabla \cdot \mathbf{U} = \left(-\frac{1}{\rho_{l}} + \frac{1}{\rho_{v}} \right) \dot{m}. \tag{11}$$

If there were no phase change source terms, the divergence of velocity would have been zero. Since it is not zero, closure is needed by computing the mass transfer term.

The divergence of the semi-discretised form of the momentum equation is given by

$$\nabla \cdot \left(\frac{\mathbf{H}(\mathbf{U})}{a_p}\right) - \nabla \cdot \left(\frac{1}{a_p} \nabla p\right) = \nabla \cdot \mathbf{U},\tag{12}$$

which is used to construct the pressure equation by substitution into the continuity equation. For this derivation and the definition of a_p and $\mathbf{H}(\mathbf{U})$, please refer to Jasak [12]. As shown earlier, the divergence of \mathbf{U} is the mass transfer rate term, so Eqn. 12 can be written as

$$\nabla \cdot \left(\frac{\mathbf{H}(\mathbf{U})}{a_p}\right) - \nabla \cdot \left(\frac{1}{a_p} \nabla p\right) = \left(-\frac{1}{\rho_l} + \frac{1}{\rho_v}\right) \dot{m}. \tag{13}$$

There is also a need for closure in the pressure equation by computing the mass transfer rate terms. This is done using a cavitation model described in the following section.

2.2. Cavitation model. To close the mathematical system above, a model is needed for the mass transfer rates. In this study, a modified version of the Schnerr and Sauer [13] model is used. The modification was originally done by Yuan and Schnerr [9]. The model is based on the idea that for cavitation to take place, it has to have a place to begin. The starting place is defined as an amount of small bubble nuclei present in the liquid phase. The mass transfer rate terms are quantified in terms of the growth and collapse of these nuclei. For the modified Schnerr and Sauer model, the mass transfer terms are given by

$$\dot{m}_{\rm ac} = -C_{\rm c} \left(\frac{\rho_{\rm v} \rho_{\rm l}}{\rho + \alpha_{\rm nc} \left(\rho_{\rm l} - \rho_{\rm nc} \right)} \right) \frac{3\alpha_{\rm v} \sqrt{\frac{2}{3\rho_{\rm l}}} \sqrt{\frac{1}{|p - p_{\rm sat}|}} \max(p - p_{\rm sat}, 0)}{\left(\frac{\rho + \alpha_{\rm nc} \left(\rho_{\rm v} - \rho_{\rm nc} \right)}{\rho + \alpha_{\rm nc} \left(\rho_{\rm l} - \rho_{\rm nc} \right)} \right) \frac{4}{3} \pi n_0 R^4 + R} \text{ if } p \ge p_{\rm sat},$$

$$(14)$$

$$\dot{m}_{\rm av} = -C_{\rm v} \left(\frac{\rho_{\rm v} \rho_{\rm l}}{\rho + \alpha_{\rm nc} \left(\rho_{\rm l} - \rho_{\rm nc} \right)} \right) \frac{\alpha_{\rm l} 4 n_0 \pi R^2 \sqrt{\frac{2}{3\rho_{\rm l}}} \sqrt{\frac{1}{|p - p_{\rm sat}|}} \min(p - p_{\rm sat}, 0)}{1 + n_0 \frac{4}{3} \pi R^3 \left(\frac{\rho + \alpha_{\rm nc} (\rho_{\rm v} - \rho_{\rm nc})}{\rho + \alpha_{\rm nc} (\rho_{\rm l} - \rho_{\rm nc})} \right)} \text{ if } p < p_{\rm sat}.$$
 (15)

These equations are used to represent the mass transfer rates in Eqn. 6 and Eqn. 7. R is the radius of the bubble nuclei and p_{sat} is the saturation pressure of the fluid. C_c and C_v are experimental constants

used to balance the two different terms. The radius of the bubbles is given by

$$R = \sqrt[3]{\frac{3}{4\pi n_0} \frac{1 + \alpha_{\text{nuc}} - \alpha_l}{\alpha_l}},\tag{16}$$

where the subscript nuc refers to the initial bubble nuclei. α_{nuc} is the volume fraction of the initial bubble nuclei, defined as

$$\alpha_{\text{nuc}} = \frac{V_{\text{nuc}}}{1 + V_{\text{nuc}}} = \frac{\frac{\pi n_0 d_{\text{nuc}}^3}{6}}{1 + \frac{\pi n_0 d_{\text{nuc}}^3}{6}}.$$
(17)

This is a result of the main assumption in the Schneer and Sauer model stated here as

$$\alpha_{\rm v} = \alpha_{\rm l} n_0 \frac{4}{3} \pi R^3,\tag{18}$$

which defines the liquid as always having a small number of bubble nuclei present. The mass transfer terms, together with the bubble radius, close the mathematical system. The following section describes how the equations are manipulated and implemented into the code.

3. Implementation

To make the mathematical system of the volume fraction equations more stable, some manipulation is done, so the source terms in Eqn. 14 and Eqn. 15 can be taken into account in a semi-implicit manner. This section outlines this manipulation so the reader to more easily understand the source code. The detailed derivation of the source terms from Appendix A.1 led to Eqn. 57, restated here as

$$\frac{d\alpha_{\rm v}}{dt} = \begin{cases}
\frac{3\alpha_{\rm v}\frac{dR}{dt}}{\left(\frac{\rho + \alpha_{\rm nc}(\rho_{\rm v} - \rho_{\rm nc})}{\rho + \alpha_{\rm nc}(\rho_{\rm l} - \rho_{\rm nc})}\right)\frac{4}{3}\pi n_0 R^4 + R} & \text{if } p \ge p_{\rm sat} \\
\frac{\alpha_1 4 n_0 \pi R^2 \frac{dR}{dt}}{1 + n_0 \frac{4}{3}\pi R^3 \left(\frac{\rho + \alpha_{\rm nc}(\rho_{\rm v} - \rho_{\rm nc})}{\rho + \alpha_{\rm nc}(\rho_{\rm l} - \rho_{\rm nc})}\right)} & \text{if } p < p_{\rm sat}.
\end{cases}$$
(19)

To close the mathematical system, the term for $\frac{dR}{dt}$ needs to be determined. For this the simplified Rayleigh equation is used [14], shown here as

$$\frac{dR}{dt} = \sqrt{\frac{2}{3} \frac{p_{\text{sat}} - p}{\rho}}.$$
 (20)

Equation 20 is implemented for the growth and collapse terms as

$$\frac{dR}{dt} = \begin{cases}
-\max(p - p_{\text{sat}}, 0) \sqrt{\frac{2}{3} \frac{1}{\rho_{\text{l}} | p - p_{\text{sat}}|}} & \text{if } p \ge p_{\text{sat}} \\
-\min(p - p_{\text{sat}}, 0) \sqrt{\frac{2}{3} \frac{1}{\rho_{\text{l}} | p - p_{\text{sat}}|}} & \text{if } p < p_{\text{sat}}.
\end{cases}$$
(21)

To get the source terms on a form that can be taken into account in a semi-implicit manner, they have to be manipulated a bit. Since the term $\frac{d\alpha_v}{dt}$ from Eqn. 43 from Appendix A is the sum of the two cases in Eqn. 19, it can be written as a sum of the two as

$$\frac{d\alpha_{\rm v}}{dt} = \alpha_{\rm v} \left. \frac{d\alpha_{\rm v}}{dt} \right|_{\rm cond} + \alpha_{\rm l} \left. \frac{d\alpha_{\rm v}}{dt} \right|_{\rm evap} = \left(\left. \frac{d\alpha_{\rm v}}{dt} \right|_{\rm evap} - \left. \frac{d\alpha_{\rm v}}{dt} \right|_{\rm cond} \right) \alpha_{\rm l} + \left. \frac{d\alpha_{\rm v}}{dt} \right|_{\rm cond} (1 - \alpha_{\rm nc}). \tag{22}$$

Here $\frac{d\alpha_{\rm v}}{dt}\big|_{\rm cond}$ and $\frac{d\alpha_{\rm v}}{dt}\big|_{\rm evap}$ are calculated using the two cases from Eqn. 19, but excluding $\alpha_{\rm l}$ and $\alpha_{\rm v}$. Utilising Eqn. 22 allows for the discretisation of everything multiplied with $\alpha_{\rm l}$ implicitly and the rest explicitly. To further stabilise the transport equations for the volume fraction, $\alpha_{\rm l}\nabla\cdot\mathbf{U}$ is added and subtracted on the right-hand side so the transport equation for $\alpha_{\rm l}$ becomes

$$\frac{\partial \alpha_{l}}{\partial t} + \nabla \cdot (\mathbf{U}\alpha_{l}) = -\frac{\rho_{v}}{\rho + \alpha_{nc} (\rho_{l} - \rho_{nc})} \frac{d\alpha_{v}}{dt} - \alpha_{l} \frac{(\rho_{l} - \rho_{v})}{\rho + \alpha_{nc} (\rho_{l} - \rho_{nc})} \frac{d\alpha_{v}}{dt} + \alpha_{l} \nabla \cdot \mathbf{U}. \tag{23}$$

In Eqn. 23, Eqn. 43 and Eqn. 44 from Appendix A have been substituted into the transport equation. Rearranging yields

$$\frac{\partial \alpha_{l}}{\partial t} + \nabla \cdot (\mathbf{U}\alpha_{l}) = \frac{\rho_{v}\rho_{l}}{\rho + \alpha_{nc} \left(\rho_{l} - \rho_{nc}\right)} \frac{d\alpha_{v}}{dt} \left[-\frac{1}{\rho_{l}} + \alpha_{l} \left(\frac{1}{\rho_{l}} - \frac{1}{\rho_{v}} \right) \right] + \alpha_{l}\nabla \cdot \mathbf{U}. \tag{24}$$

Here the term $\frac{d\alpha_{\rm v}}{dt}$ is calculated using Eqn. 22. This is the implemented form of the transport equation for $\alpha_{\rm l}$ which is solved together with the transport equation for $\alpha_{\rm nc}$ and the system is closed using Eqn. 2. The code implementation of the volume fraction equation for $\alpha_{\rm l}$ can be seen in Listing 1 below:

```
1
        fvScalarMatrix alpha1Eqn
2
3
            fv::EulerDdtScheme<scalar>(mesh).fvmDdt(alpha1)
4
            fv::gaussConvectionScheme<scalar>
5
6
                mesh,
7
                phi,
8
                upwind<scalar>(mesh, phi)
9
            ).fvmDiv(phi, alpha1)
10
            fvm::Sp(divU, alpha1)
11
12
            fvm::Sp(vDotvmcAlphal, alpha1)
13
            vDotcAlphal*(1.0-alpha3)
14
        );
```

Listing 1. Implementation of the volume fraction equation for the liquid phase.

3.1. Pressure correction equation. The pressure correction equation shown in Eqn. 13 also has a mass flow term on the right-hand side. To mathematically close the system, the source terms from the cavitation model are needed again. Since the pressure correction equation is using the modified pressure $\hat{p} = p - \rho(\mathbf{g} \cdot \mathbf{h})$ and because the source terms from the cavitation model are based on $p - p_{\text{sat}}$, $p - p_{\text{sat}}$ is rewritten as

$$p - p_{\text{sat}} - \rho(\mathbf{g} \cdot \mathbf{h}) + \rho(\mathbf{g} \cdot \mathbf{h}) = \hat{p} - p_{\text{sat}} + \rho(\mathbf{g} \cdot \mathbf{h}). \tag{25}$$

By using Eqn. 43 from Appendix A, the source terms from the cavitation model are rewritten as

$$\dot{m} = \frac{(\rho_{\rm l} - \rho_{\rm v})}{\rho + \alpha_{\rm nc} (\rho_{\rm l} - \rho_{\rm nc})} \cdot \begin{cases} -\frac{3\alpha_{\rm v} \sqrt{\frac{2}{3\rho_{\rm l}}} \sqrt{\frac{1}{|p-p_{\rm sat}|} \cdot pos0(p-p_{\rm sat})}}{\left(\frac{\rho + \alpha_{\rm nc}(\rho_{\rm v} - \rho_{\rm nc})}{\rho + \alpha_{\rm nc}(\rho_{\rm l} - \rho_{\rm nc})}\right) \frac{4}{3} \pi n_0 R^4 + R} & \text{if } p \ge p_{\rm sat} = \dot{m}_+ \\ \frac{\alpha_{\rm l} 4 n_0 \pi R^2 \sqrt{\frac{2}{3\rho_{\rm l}}} \sqrt{\frac{1}{|p-p_{\rm sat}|} \cdot neg(p-p_{\rm sat})}}{1 + n_0 \frac{4}{3} \pi R^3 \left(\frac{\rho + \alpha_{\rm nc}(\rho_{\rm v} - \rho_{\rm nc})}{\rho + \alpha_{\rm nc}(\rho_{\rm l} - \rho_{\rm nc})}\right)} & \text{if } p < p_{\rm sat} = \dot{m}_-. \end{cases}$$

$$(26)$$

In Eqn. 26, pos0 and neg are used instead of the min/max functions, so the source terms can be multiplied by Eqn. 25. Since the min function from Eqn. 15 would normally give a negative value or 0, the minus from the case of $p < p_{\rm sat}$ in Eqn. 26 is removed. As for the case of the volume fraction equations, the total mass flow is a sum of the two cases from Eqn. 26. The final form of the mass flow term for the pressure correction equation is defined as

$$\dot{m} = [p_{\text{sat}} - \rho(\mathbf{g} \cdot \mathbf{h})] (\dot{m}_{-} - \dot{m}_{+}) - (\dot{m}_{-} - \dot{m}_{+}) \hat{p}. \tag{27}$$

This is what is implemented for the pressure equation shown in Listing 2.

Listing 2. Implementation of the modified pressure equation.

4. Benchmark

The benchmark case used was first proposed by Giussani et al. [10] and was also employed by Aqeel [15]. The domain used for the benchmark, together with some of the boundary and initial conditions, are shown in Fig. 1. The mesh of the case is $1 \times 640 \times 1$ cells large on a domain that is 2 m tall with the y coordinate facing opposite gravity. The benchmark is split into two sections, one where only cavitation is taking place and one where only condensation is. The initial conditions for both cases are shown in Tab. 1. Generally, the boundary and initial conditions are set to allow for calculations in 1D. The vertical walls are set to slip to not interfere with the moving interfaces. The bottom of the column is a wall, and the top is an inlet-outlet. The detailed boundary conditions are shown in Tab. 2. The three phases are initialised at rest as a column stacked on top of each other with $\alpha_{\rm l}$ at the bottom and $\alpha_{\rm nc}$ at the top. For the first part of the benchmark case, $C_{\rm c}$ is set to 0, and $C_{\rm v}$ is set to 1. The opposite is done for the second part. The reason for this is to isolate the source terms and to reveal how they perform, given a similar driving

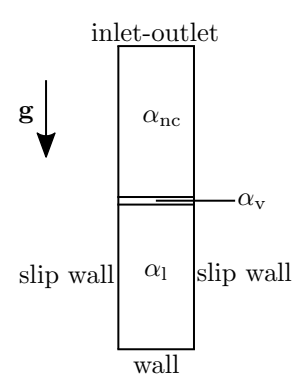


Figure 1. Schematic overview of the computational domain for the benchmark case including boundary and initial conditions.

Table 1. Initial condition for both halves of the benchmark case.

Cavitation case	Condensation case
$\alpha_{\rm l}$ from 0 to 0.95 in height	α_1 mapped from cavitation case
$\alpha_{\rm v}$ from 0.95 to 1 in height	$\alpha_{\rm v}$ mapped from cavitation case
$\alpha_{\rm nc}$ from 1 to 2 in height	$\alpha_{\rm nc}$ mapped from cavitation case
$p_{\rm sat} = 100300 \; {\rm Pa}$	$p_{\rm sat} = 99700 \; {\rm Pa}$
U = 0 m/s	U = 0 m/s
p = hydrostatic pressure	p = hydrostatic pressure
$C_{\rm c} = 0$ and $C_{\rm v} = 1$	$C_{\rm c} = 1$ and $C_{\rm v} = 0$
Nuclei density = $10^8 / \text{m}^3$	Nuclei density = $10^8 / \text{m}^3$
Nuclei diameter = 10^{-6} m	Nuclei diameter = 10^{-6} m

Table 2. Overview of boundary conditions used for the two parts of the benchmark case. Boundaries not described here are empty.

Field	top	bottom	verticalWall
alpha.air	inletOutlet	zeroGradient	zeroGradient
alpha.liquid	fixedValue	zeroGradient	zeroGradient
alpha.vapour	fixedValue	zeroGradient	zeroGradient
p	calculated	calculated	calculated
p_{rgh}	prghTotalPressure	${\it fixedFluxPressure}$	${\it fixedFluxPressure}$
\mathbf{U}°	pressureDirectedInletOutletVelocity	noSlip	slip

potential. The fluid properties used for the simulations are the same as those used for the famous rising bubble benchmark case. The fluid properties are shown in Tab. 3. Besides the initial condition and the

Table 3. Fluid properties used for the two benchmark cases.

Property	Unit
$\overline{\rho_{\mathrm{l}}}$	1000 kg/m^3
$\rho_{\rm v} = \rho_{\rm nc}$	1 kg/m^3
$\sigma_{\mathrm{lv}} = \sigma_{\mathrm{vnc}}$	$1.96 \; { m N/m}$
$\mu_{ m l}$	10 kg/(m s)
$\mu_{\rm v} = \mu_{\rm nc}$	0.1 kg/(m s)
g	$(0 - 0.98 \ 0) \ m/s^2$

fluid properties, the initial pressure field is set as

$$p(y) = p_0 + \rho \mathbf{g}(h_{ref} - y). \tag{28}$$

In Eqn. 28, h_{ref} is with reference to the lower wall and is equal to 2 m, y is the y-coordinates of the cells, and p_0 is the initial pressure of 100000 Pa. To evaluate the performance of the implemented code, several quantities are tracked in the benchmark case. They are shown in Eqn. 29 to Eqn. 32. The first

parameter tracked is the mass of each fluid in the system as

$$m_i = \sum \alpha_i \rho_i V_i, \tag{29}$$

where the subscript $_{\rm i}$ refers to the value of the variable in the i'th cell. The same definition of $_{\rm i}$ is used for Eqn. 30 and Eqn. 31. The interface height for both interfaces in the system is calculated as

$$h_{\text{lv}} = \frac{\sum y_i \alpha_{\text{l},i} (1 - \alpha_{\text{l},i}) V_i}{\sum \alpha_{\text{l},i} (1 - \alpha_{\text{l},i}) V_i}, \qquad h_{\text{vnc}} = \frac{\sum y_i \alpha_{\text{nc},i} (1 - \alpha_{\text{nc},i}) V_i}{\sum \alpha_{\text{nc},i} (1 - \alpha_{\text{nc},i}) V_i}.$$
(30)

The velocity of the two interfaces is tacked as

$$\mathbf{u}_{\text{lv}} = \frac{\sum \mathbf{U}_{i} \alpha_{\text{l},i} (1 - \alpha_{\text{l},i}) V_{i}}{\sum \alpha_{\text{l},i} (1 - \alpha_{\text{l},i}) V_{i}}, \qquad \mathbf{u}_{\text{vnc}} = \frac{\sum \mathbf{U}_{i} \alpha_{\text{nc},i} (1 - \alpha_{\text{nc},i}) V_{i}}{\sum \alpha_{\text{nc},i} (1 - \alpha_{\text{nc},i}) V_{i}}.$$
(31)

The mass conservation error for each time step is calculated as

$$e_{\text{step}} = \frac{|[m_{\text{l}}(t+1) - m_{\text{l}}(t)] - [m_{\text{v}}(t+1) - m_{\text{v}}(t)]|}{m_{\text{l}}(t_0)},$$
(32)

where m is the mass of the phase, t+1 refers to the next time step, t refers to the current time step, and t_0 refers to the start of the simulation. Lastly, the global mass conservation error in percent is calculated as

$$e_{\text{global}} = \frac{|[m_{l}(t_{f}) - m_{l}(t_{0})] - [m_{v}(t_{f}) - m_{v}(t_{0})]|}{m_{l}(t_{0})} 100,$$
(33)

where $t_{\rm f}$ refers to the final time step of the simulation. Equation 29 to Eqn. 32 are evaluated during the simulation and Eqn. 33 after. The results of this are presented in the following section.

4.1. Cavitation results. The simulation starts from a hydrostatic pressure distribution given by Eqn. 28. Since the saturation pressure in the simulation is set at a value larger than the pressure boundary condition, the liquid starts to cavitate, creating more vapour. The vapour then forces the air out of the top of the column. This is also shown in Fig. 2. As the mass of the liquid starts to disappear and vapour starts

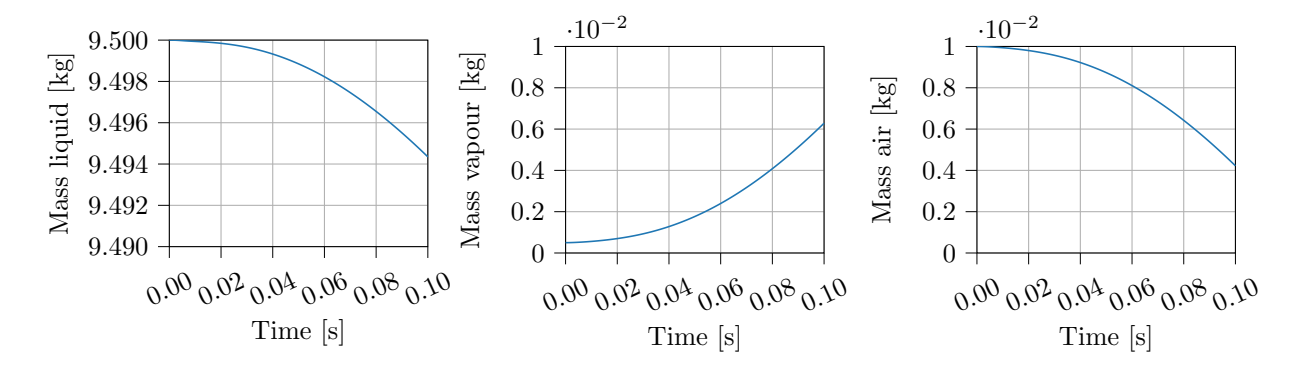


Figure 2. Temporal evolution of the mass of the 3 fluids present in the simulation.

being created, the surfaces of the interfaces between the fluids also move. The height of these interfaces is shown in Fig. 3. As seen from Fig. 3, the interface height between the liquid and vapour rises to a level higher than at the beginning of the simulation. This is due to numerical diffusion between the liquid and vapour. Since the model implemented in this study contains no artificial interface compression, the interfaces are subject to numerical diffusion. The liquid and vapour have different fluid properties, which induce instabilities in the interface stretching towards the exit as the vapour moves. The vapour and air interface rises to almost 1.6 m, meaning that roughly 60% of the air in the domain has been pushed out. The velocity of the interfaces is shown in Fig. 4. As seen from Fig. 4, the velocity of the vapour and air interface reaches a speed of approximately 12.5 m/s. This high speed pulls the rest of the vapour with it, which then pulls the liquid enough to pull the interface up a little, as also seen from Fig. 3. The mass of all the fluids in the simulation was also tracked to calculate the mass relative error during the simulation. The results are shown in Fig. 5. The mass relative error starts out at a very low value and then starts to rise. This is expected behaviour due to the initial conditions of the simulation. After about 0.03 s, the error stabilises at around $0.6 \cdot 10^{-4}\%$. This is due to the transient simulation reaching a balance in the mass transfer source terms as velocity and pressure are solved to the correct values. The mass relative error for the cavitation case is small, and therefore, the mass of the system is conserved for the cavitation

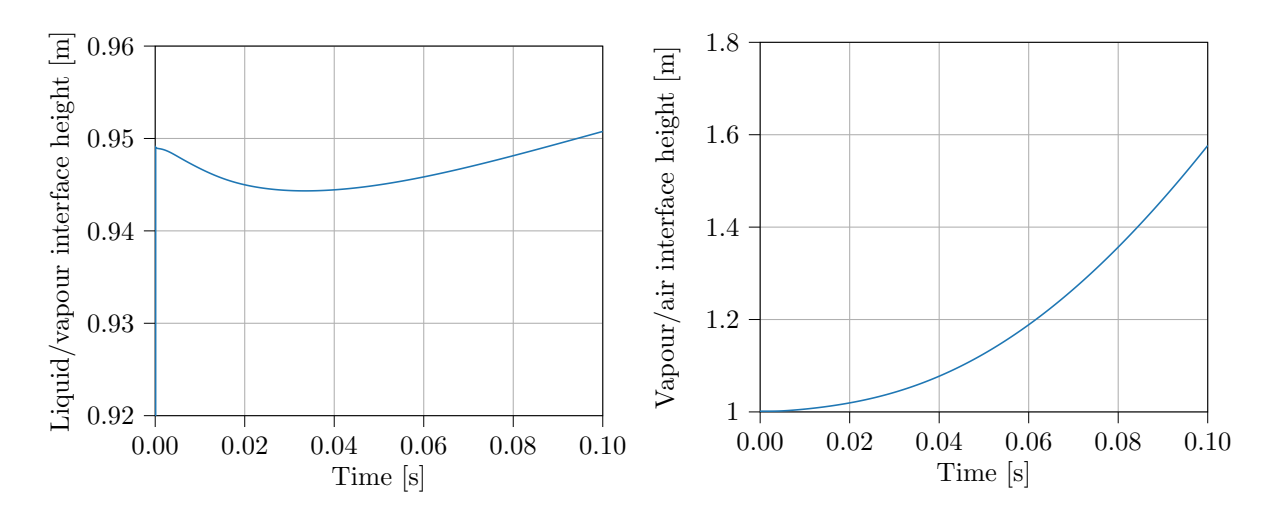


Figure 3. Height with respect to the bottom of the column of the two interface pairs present in the simulation.

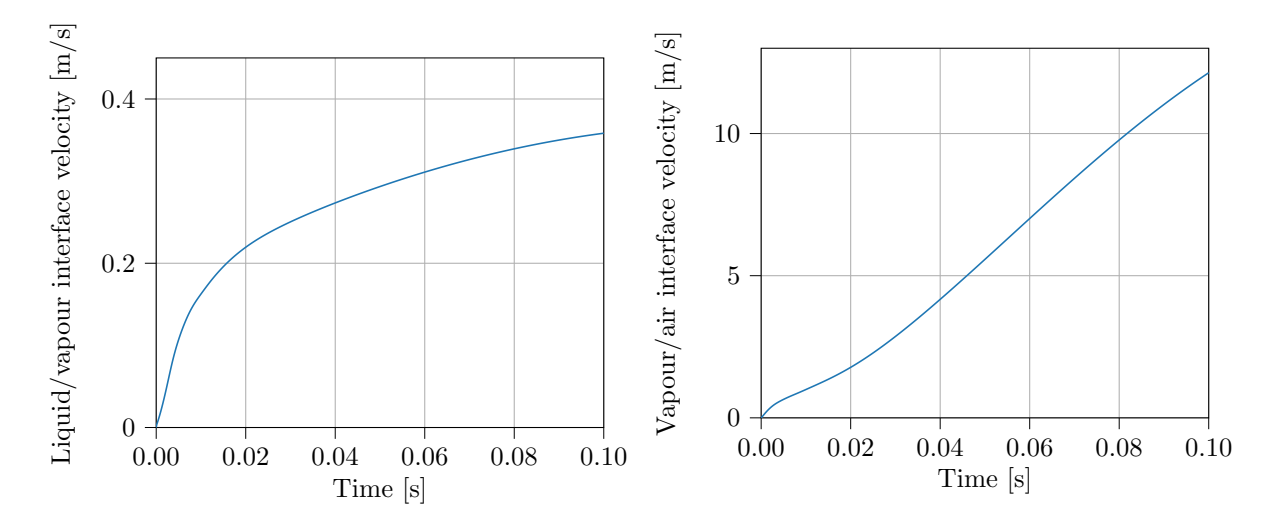


Figure 4. Velocity of the two interface pairs present in the simulation.

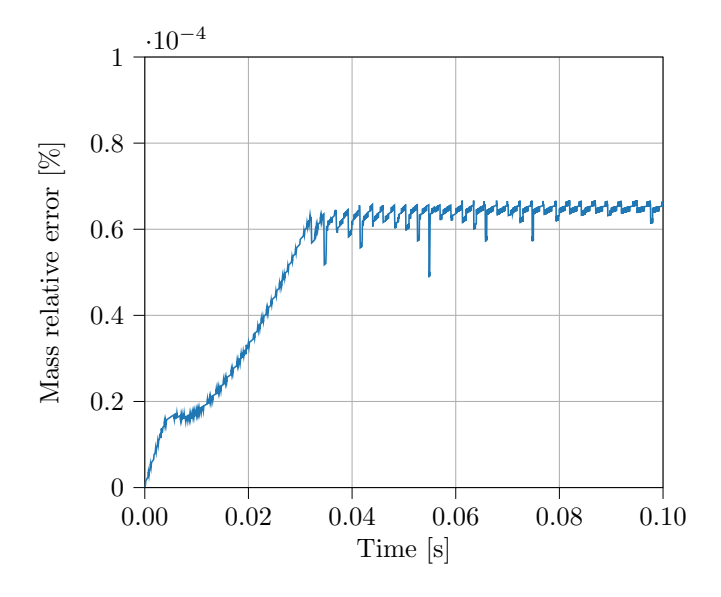


Figure 5. Mass relative error during the cavitation simulation.

terms when transfer happens between two fluids. The global mass error is 0.12039% which is close to the 0.11301% presented by [10]. The two implementations employ different solution algorithms, which is believed to be why they differ. An example of this is that the current implementation closes the system with $\alpha_{\rm v}$, whereas [10] solve the volume fraction equations separately and add the remaining error to $\alpha_{\rm nc}$. Since the mass relative error and the global mass relative error are so small, the implementation of the cavitation mass transfer term is acceptable.

4.2. Condensation results. The cavitation part of the implementation was verified, so the next step is verifying the condensation part. The same parameters are tracked for the condensation part of the benchmark case. The final solution from the cavitation part is used for the initial conditions for the condensation part. The settings are adjusted so that only the condensation term is used in the mass transfer evaluation. The mass of each fluid in the system is shown in Fig. 6. As the mass of the vapour

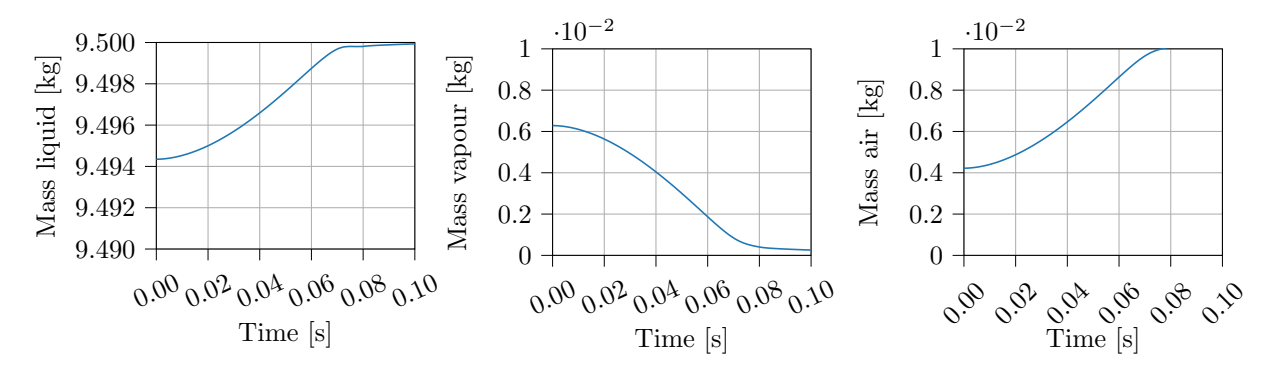


Figure 6. Temporal evolution of the mass of the three fluids present in the simulation.

starts to disappear, more liquid is being created. The layer of vapour separating the air from the liquid starts to shrink and pulls air in from the top of the column. This can also be seen from the mass evolution shown in Fig. 6. The amount of liquid almost reaches the same amount set as the initial conditions for the cavitation part of the benchmark case. The vapour mass falls below the small amount initialised for cavitation. This indicates that the condensation process is faster than cavitation. If there was a mass conservation error of 0%, the mass of the liquid would go above 9.5 kg, but since a small amount of mass is lost and not all the vapour condensates, this is not the case. The mass of the air does, however, rise above the initial level as more vapour condensates. The evolution of the height of the interfaces is shown in Fig. 7. Figure 7 shows that the liquid and vapour interface height starts moving upwards at the

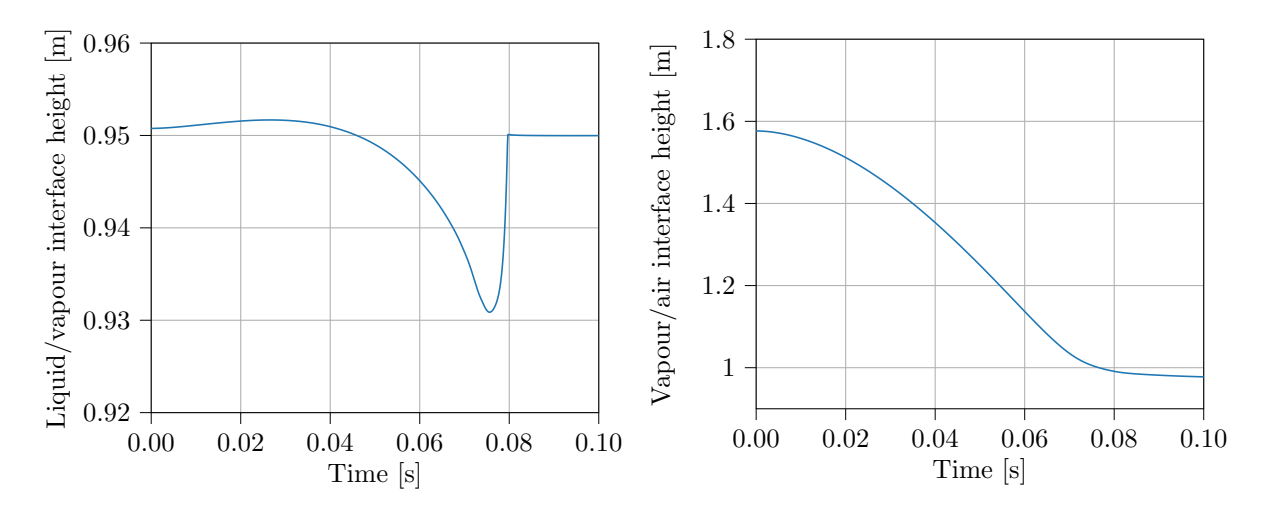


Figure 7. Height with respect to the bottom of the column of the two interface pairs present in the simulation.

beginning of the simulation. This is still due to numerical diffusion and the difference in fluid properties that cause interface instability. After roughly 0.08 s, the condensation is mostly complete as the surface height of the liquid and vapour interface is back to where it was initially. This corresponds well with the

vapour and air interface, which slowly decreases from 0.08 s as the last bit of vapour condenses. The interface velocity is shown in Fig. 8. The interface velocities are now negative as the bulk movement of the

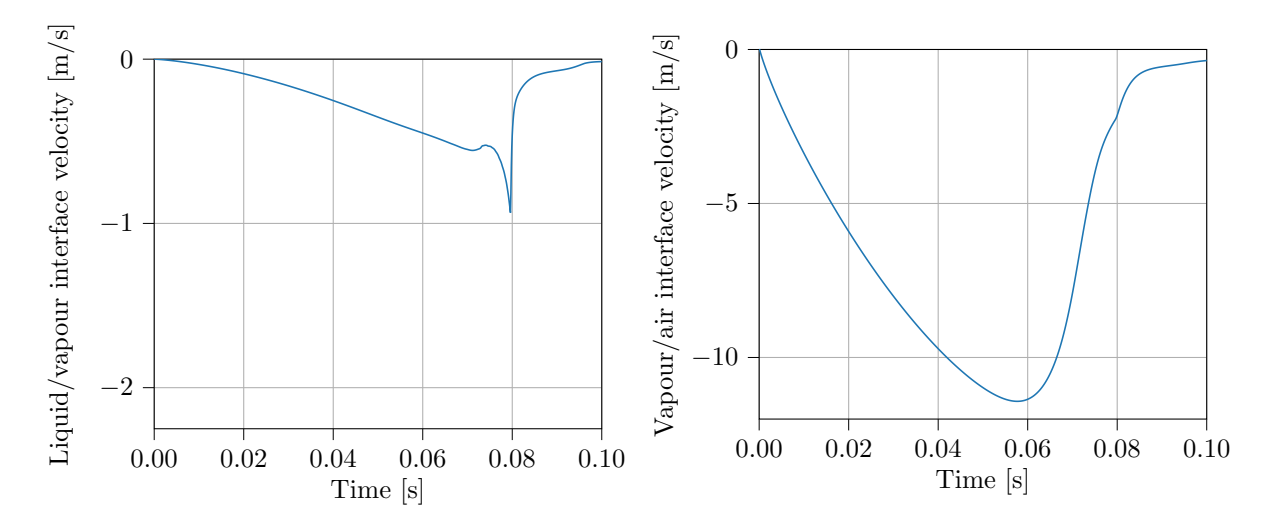


Figure 8. Velocity of the two interface pairs present in the simulation.

system is downwards. As seen from Fig. 8, the velocity starts at 0 when the interfaces are initially at rest and then decreases as the fluid moves downwards. Again, the magnitude of the velocity is much greater for the vapour and air interface than for the vapour and liquid interface. This is due to the difference in fluid properties. The velocity increases at 0.08 s as the vapour and air interface almost reaches the liquid and vapour. From that point, the interfaces drastically slow down as the condensation is almost over, and therefore, the driving potential is removed.

The mass relative error for the condensation case is shown in Fig. 9, which shows that the mass relative error rises in the beginning to about the same value as the condensation case. The first rise from 0 s to

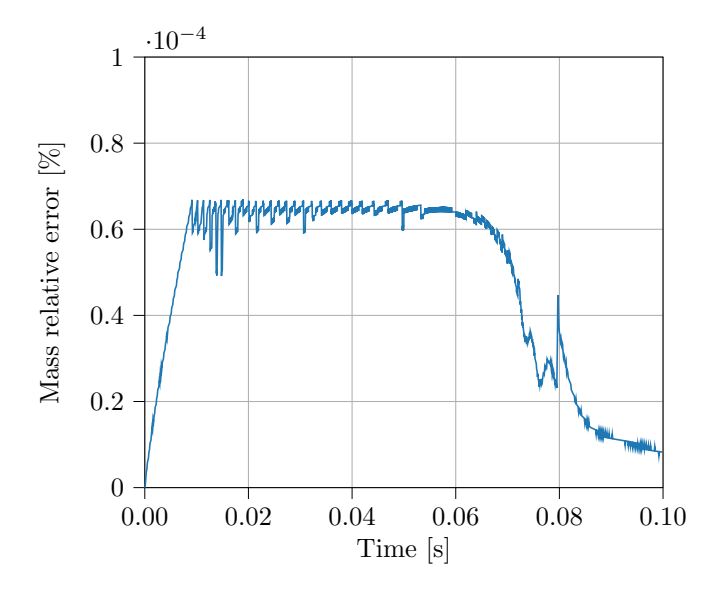


Figure 9. Mass relative error during the cavitation simulation.

0.01 s is again due to initial conditions. From there, the mass relative error is steady until about 0.07 s, where it begins to reduce as the mass transfer rate falls since condensation is almost over. At 0.08 s, the mass relative error spikes as the interfaces drastically slow down. From 0.08 s, the last vapour is slowly condensing and the error drops accordingly. The global mass error is 0.12229% which is again close to the 0.1126% from [10]. The reason for the difference is believed to be the difference in algorithms between the two implementations. For the condensation case, the mass relative error and the global mass error are around the same magnitude as for the cavitation case. This means that the mass is conserved.

5. Nozzle simulation

The case used for validation is the one from Sou et al. [16] and Bicer and Sou [17]. The simulation of the internal nozzle flow is performed to evaluate how the implemented solver performs on a well-documented geometry with internal cavitation in the nozzle. The simulated injector is transparent, and velocity measurements of the inside flow were obtained using laser doppler velocity (LDV). The simulated domain is shown in Fig. 10, which depicts the flow entering the inlet and exiting the outlet. Every side on

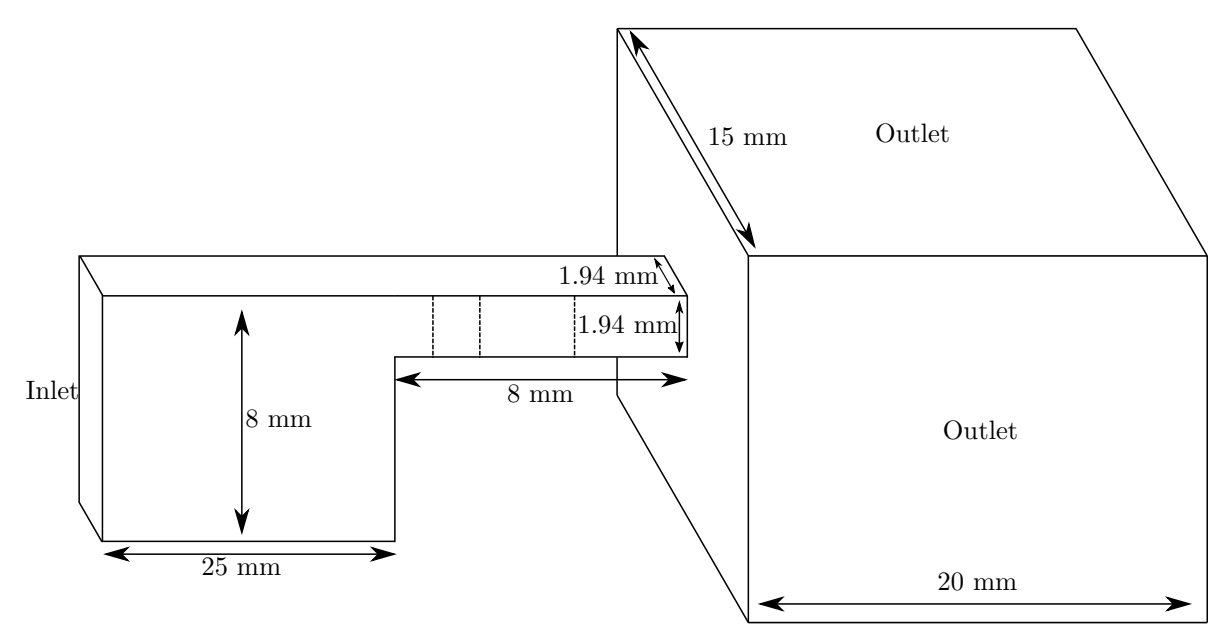


Figure 10. Schematic of the geometry of the injector. Measurement locations for the LDV measurements are marked with dotted lines and are located 1.5 mm, 3 mm and 6 mm into the 8 mm long nozzle.

the outlet box except the side where the nozzle is connected is considered an outlet in terms of boundary conditions. Every boundary that is neither an outlet nor an inlet is considered a wall. In Fig. 10, the locations for the LDV measurements are marked with dotted lines. The measurements were taken in the centreline of the nozzle at 1.5 mm, 3 mm and 6 mm into the nozzle throat. The nozzle sprays water into an air-filled reservoir, and the physical parameters of the fluids in the domain are defined as shown in Tab. 4. The simulation is performed with a volumetric flowrate of $4.8 \cdot 10^{-5}$ m³/s as an inlet condition,

Table 4. Physical properties of the fluids in the simulation.

Fluid	Density	Kinematic viscosity	Surface tension	Saturation pressure
Water	998kg/m^3	$1.2 \cdot 10^{-6} \text{ m}^2/\text{s}$	$0.07 \; \mathrm{N/m}$	2300 Pa
Vapour	0.739 kg/m^3	$1.6614 \cdot 10^{-5} \text{ m}^2/\text{s}$		
Air	$1.19 \mathrm{kg/m^3}$	$1.4496 \cdot 10^{-5} \text{ m}^2/\text{s}$		

and the pressure is set on the outlet boundary to 1 bar. The cavitation number of the simulation is 1.2, which means the flow is in the developing cavitation regime. The number of initial nuclei for the cavitation model is set to 10^{15} per cubic meter, and their initial diameter is set to 1.5μ m. Large eddy simulation (LES) turbulence modelling is employed via the WALE model [18]. The computational mesh is shown in Fig. 11. The mesh contains about 4.5 million cells, which are mainly located in the throat of the nozzle. The walls in the domain have been refined to have a first cell height of 2.5 μ m to give a Courant–Friedrichs–Lewy (CFL) number of approximately 1. The mesh has fairly large cells in the regions outside the throat, which results in the interfaces being very smeared in those regions. This drastically reduces the number of cells and thus reduces computational time. The simulation is run for 3 ms to develop the flow and 2 ms with field averaging turned on afterwards. The field averaged velocity in the injection direction at the LDV locations is compared with experimental results from Sou et al. [16]. This is presented in Fig. 12. Figure 12 demonstrates quite a good agreement between the simulation and the experimental values. At the first measurement location, 1.5 mm into the nozzle throat, the model is able to capture the recirculation zone that appears when the fluid is separated from the sharp corner at



Figure 11. Slice of the mesh used in the simulation. Slice is of the refined region of the domain.

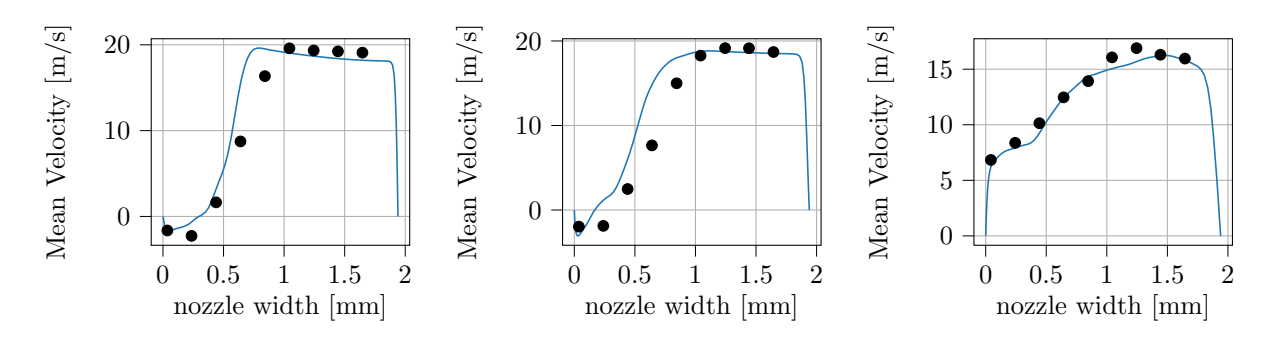


Figure 12. Comparison of the experimental measurements (•) from Sou et al. [16] and the averaged velocity from the simulation in the injection direction. The three figures are from the (left to right) 1.5 mm, 3 mm and 6 mm measurement lines, respectively.

the entrance to the throat. The velocity of the bulk flow is also captured quite well. At 3 mm into the throat, the recirculation zone is smaller in size. Looking at the model prediction, the negative part of the velocity covers a smaller part of the nozzle width. The bulk flow velocity is still predicted quite well at 3 mm. Common for both the 1.5 mm and 3 mm measurement zones is that the width of the recirculation zone predicted by the model is smaller than what is observed experimentally. Due to this, the transition from the recirculation zone to bulk flow is not quite in the same location as observed experimentally. At the 6 mm measurement zone, the recirculation zone is gone. The vapour created in the recirculation zone has condensed again. The agreement between the measurements and the simulation is good, indicating that the length of the recirculation zone is predicted quite well. A comparison of the vapour created and a photograph taken by Sou et al. [16] is shown in Fig. 13. As seen in Fig. 13, the length the water vapour reaches into the nozzle in the simulation agrees quite well with what is observed experimentally. Even though no artificial interface compression is used in the current implementation, the vapour pockets are quite well-defined.

6. Conclusion

This study implemented an extension to interPhaseChangeFoam with a modified SchnerrSauer cavitation model. The implemented model can consider the nozzle's internal cavitation effects on the breakup of the liquid. The solver is verified on a benchmark case proposed by Giussani et al. [10] consisting of a one-dimensional liquid, vapour and air column. The case consists of two parts and is designed to evaluate



Figure 13. Comparison of an instantaneous iso-contour of $\alpha_{water} = 0.5$ to photography from Sou et al. [16]. Boundaries of the internal geometry of the nozzle are outlined in black.

the mass conservation of a VoF solver with mass transfer. The implemented solver can solve both parts of the first case with a mass relative error below 0.00007 %. The solver is validated for real nozzle flow and compared to the experiments from the literature performed on the same geometry. The implemented model is revealed through comparison with flow images to capture the size and location of the cavitation vapour bubbles well. The velocity predicted by the implemented model closely follows the experimental measurements at three different locations in the nozzle, and the model captures the recirculation zones induced by the geometry.

Acknowledgements

The research leading to these results has received funding from the Danish Innovation Foundation under grant no. 9065-00197B.

Author Contributions: Conceptualisation, B.C.D.; methodology, B.C.D.; software, B.C.D.; validation, B.C.D.; formal analysis, B.C.D.; investigation, B.C.D.; resources, B.C.D. and J.H.; data curation, B.C.D.; writing—original draft preparation, B.C.D.; writing—review and editing, J.H. and J.d.C.C and B.E. and N.K.; visualisation, B.C.D.; supervision, J.H. and J.d.C.C and B.E. and N.K.; project administration, J.d.C.C and B.E. and N.K.; funding acquisition, J.d.C.C and B.E. and N.K.. All authors have read and agreed to the published version of the manuscript.

Appendix A. Derivation of modified Schneer and Sauer model

The system of equations is

$$\begin{split} \frac{\partial \alpha_{l}}{\partial t} + \nabla \cdot (\alpha_{l} \mathbf{U}) &= -\frac{\dot{m}}{\rho_{l}}, \\ \frac{\partial \alpha_{v}}{\partial t} + \nabla \cdot (\alpha_{v} \mathbf{U}) &= \frac{\dot{m}}{\rho_{v}}, \\ \frac{\partial \alpha_{nc}}{\partial t} + \nabla \cdot (\alpha_{nc} \mathbf{U}) &= 0. \end{split}$$

Using the definition of total derivative shown in Eqn. 34, where α_i refers to a general volume fraction, solving it for $\frac{\partial \alpha_i}{\partial t}$ and inserting it into the transport equations, Eqn. 35 can be obtained.

$$\frac{d\alpha_i}{dt} = \frac{\partial \alpha_i}{\partial t} + (\mathbf{U} \cdot \nabla)\alpha_i \tag{34}$$

$$\frac{d\alpha_i}{dt} - \mathbf{U} \cdot \nabla \alpha_i + \nabla \cdot (\mathbf{U}\alpha_i) = 0$$
(35)

Using the product rule for divergence that states $\nabla \cdot (\mathbf{U}\alpha_i) = (\nabla \alpha_i) \cdot \mathbf{U} + \alpha_i \nabla \cdot \mathbf{U}$ together with the commutative property that $(\nabla \alpha_i) \cdot \mathbf{U} = \mathbf{U} \cdot (\nabla \alpha_i)$. Eqn. 35 can rewritten as

$$\frac{d\alpha_{l}}{dt} + \alpha_{l}\nabla \cdot (\mathbf{U}) = -\frac{\dot{m}}{\rho_{l}},\tag{36}$$

$$\frac{d\alpha_{\mathbf{v}}}{dt} + \alpha_{\mathbf{v}} \nabla \cdot (\mathbf{U}) = \frac{\dot{m}}{\rho_{\mathbf{v}}},\tag{37}$$

$$\frac{d\alpha_{\rm nc}}{dt} + \alpha_{\rm nc}\nabla \cdot (\mathbf{U}) = 0. \tag{38}$$

It is used that the change of the sum of volume fractions is 0, written as

$$\frac{d\alpha_{\rm l}}{dt} + \frac{d\alpha_{\rm v}}{dt} + \frac{d\alpha_{\rm nc}}{dt} = 0. \tag{39}$$

Substituting $\frac{d\alpha_1}{dt}$ and $\frac{d\alpha_{nc}}{dt}$ from the above transport equations in Eqn. 36 and Eqn. 38 yields

$$-\alpha_{\rm l}\nabla\cdot\mathbf{U} - \frac{\dot{m}}{\rho_{\rm l}} + \frac{d\alpha_{\rm v}}{dt} - \alpha_{\rm nc}\nabla\cdot\mathbf{U} = 0$$

Solving for the mass flow rate yields

$$-\rho_{l} \left(\alpha_{l} + \alpha_{nc}\right) \nabla \cdot \mathbf{U} - \rho_{l} \frac{d\alpha_{v}}{dt} = \dot{m}. \tag{40}$$

One of terms for the mass transfer rate is obtained from the time rate of change. The other is derived by looking at the non-conservative continuity equation given by

$$\nabla \cdot \mathbf{U} = -\frac{1}{\rho} \frac{dp}{dt}.$$

Considering that each phase is incompressible, this equation can be written as

$$\begin{split} \nabla \cdot \mathbf{U} &= -\frac{1}{\rho} \left(\frac{d(\rho_{l}\alpha_{l})}{dt} + \frac{d(\rho_{v}\alpha_{v})}{dt} + \frac{d(\rho_{nc}\alpha_{nc})}{dt} \right), \\ &= -\frac{1}{\rho} \left(\rho_{l} \frac{d\alpha_{l}}{dt} + \rho_{v} \frac{d\alpha_{v}}{dt} + \rho_{nc} \frac{d\alpha_{nc}}{dt} \right). \end{split}$$

Substituting $\frac{d\alpha_1}{dt}$ and $\frac{d\alpha_{nc}}{dt}$ with Eqn. 36 and Eqn. 38 yields

$$\nabla \cdot \mathbf{U} = -\frac{1}{\rho} \left(-\rho_{l} \alpha_{l} \nabla \cdot \mathbf{U} - \dot{m} + \rho_{v} \frac{d\alpha_{v}}{dt} - \rho_{nc} \alpha_{nc} \nabla \cdot \mathbf{U} \right).$$

Rearranging to isolate for the mass transfer rate yields

$$\dot{m} = \rho_{\rm v} \frac{d\alpha_{\rm v}}{dt} + (-\rho_{\rm l}\alpha_{\rm l} - \rho_{\rm nc}\alpha_{\rm nc} + \rho) \nabla \cdot \mathbf{U}. \tag{41}$$

Equating Eqn. 40 and Eqn. 41 yields

$$(-\rho_{l}\alpha_{l} - \rho_{nc}\alpha_{nc} + \rho)\nabla \cdot \mathbf{U} + \frac{d\alpha_{v}}{dt}\rho_{v} = -\rho_{l}(\alpha_{l} + \alpha_{nc})\nabla \cdot \mathbf{U} + \frac{d\alpha_{v}}{dt}\rho_{l}.$$
(42)

Rearranging gives

$$(-\rho_{l}\alpha_{l} - \rho_{nc}\alpha_{nc} + \rho) \nabla \cdot \mathbf{U} + \rho_{l} (\alpha_{l} + \alpha_{nc}) \nabla \cdot \mathbf{U} = \frac{d\alpha_{v}}{dt} (\rho_{l} - \rho_{v}),$$

$$(-\rho_{l}\alpha_{l} - \rho_{nc}\alpha_{nc} + \rho + \rho_{l}\alpha_{l} + \rho_{l}\alpha_{nc}) \nabla \cdot \mathbf{U} = \frac{d\alpha_{v}}{dt} (\rho_{l} - \rho_{v}),$$

$$(-\rho_{nc}\alpha_{nc} + \rho + \rho_{l}\alpha_{nc}) \nabla \cdot \mathbf{U} = \frac{d\alpha_{v}}{dt} (\rho_{l} - \rho_{v}).$$

Solving for the divergence of velocity gives

$$\frac{d\alpha_{\rm v}}{dt} \frac{(\rho_{\rm l} - \rho_{\rm v})}{\rho + \alpha_{\rm nc} (\rho_{\rm l} - \rho_{\rm nc})} = \nabla \cdot \mathbf{U}.$$
(43)

If the transport equation for $\alpha_{\rm v}$ is solved for \dot{m} and Eqn. 43 is substituted into it, it yields

$$\dot{m} = \rho_{\rm v} \frac{d\alpha_{\rm v}}{dt} + \alpha_{\rm v} \rho_{\rm v} \frac{(\rho_{\rm l} - \rho_{\rm v})}{\rho + \alpha_{\rm nc} (\rho_{\rm l} - \rho_{\rm nc})} \frac{d\alpha_{\rm v}}{dt},$$

$$\dot{m} = \rho_{\rm v} \frac{d\alpha_{\rm v}}{dt} \left(1 + \frac{\alpha_{\rm v} (\rho_{\rm l} - \rho_{\rm v})}{\rho + \alpha_{\rm nc} (\rho_{\rm l} - \rho_{\rm nc})} \right),$$

$$\dot{m} = \rho_{\rm v} \frac{d\alpha_{\rm v}}{dt} \left(\frac{(\rho + \alpha_{\rm nc} \rho_{\rm l} - \alpha_{\rm nc} \rho_{\rm nc} + \alpha_{\rm v} \rho_{\rm l} - \alpha_{\rm v} \rho_{\rm v})}{\rho + \alpha_{\rm nc} (\rho_{\rm l} - \rho_{\rm nc})} \right),$$

$$\dot{m} = \rho_{\rm v} \frac{d\alpha_{\rm v}}{dt} \left(\frac{\alpha_{\rm l} \rho_{\rm l} + \alpha_{\rm v} \rho_{\rm v} + \alpha_{\rm nc} \rho_{\rm nc} + \alpha_{\rm nc} \rho_{\rm l} - \alpha_{\rm nc} \rho_{\rm nc} + \alpha_{\rm v} \rho_{\rm l} - \alpha_{\rm v} \rho_{\rm v})}{\rho + \alpha_{\rm nc} (\rho_{\rm l} - \rho_{\rm nc})} \right),$$

$$\dot{m} = \rho_{\rm v} \frac{d\alpha_{\rm v}}{dt} \left(\frac{\rho_{\rm l} (\alpha_{\rm l} + \alpha_{\rm v} + \alpha_{\rm nc})}{\rho + \alpha_{\rm nc} (\rho_{\rm l} - \rho_{\rm nc})} \right),$$

$$\dot{m} = \frac{d\alpha_{\rm v}}{dt} \left(\frac{\rho_{\rm v} \rho_{\rm l}}{\rho + \alpha_{\rm nc} (\rho_{\rm l} - \rho_{\rm nc})} \right).$$
(44)

Equation 44 and Eqn. 43 are used in the implementation of the modified cavitation model.

A.1. Condensation and evaporation terms for the modified Schneer and Sauer model. The derivation starts with the definition from the Schnerr and Sauer model restated in Eqn. 45 as

$$\alpha_{\rm v} = \alpha_{\rm l} n_0 \pi \frac{4}{3} R^3. \tag{45}$$

Taking the total derivative of Eqn. 45 yields

$$\frac{d\alpha_{\rm v}}{dt} = \alpha_{\rm l} 4\pi n_0 R^2 \frac{dR}{dt} + n_0 \frac{4}{3}\pi R^3 \frac{d\alpha_{\rm l}}{dt}.$$
(46)

The volume fraction equation system is

$$\frac{d\alpha_{l}}{dt} + \alpha_{l}\nabla \cdot (\mathbf{U}) = \frac{\dot{m}}{\rho_{l}},\tag{47}$$

$$\frac{d\alpha_{\mathbf{v}}}{dt} + \alpha_{\mathbf{v}} \nabla \cdot (\mathbf{U}) = -\frac{\dot{m}}{\rho_{\mathbf{v}}},\tag{48}$$

$$\frac{d\alpha_{\rm nc}}{dt} + \alpha_{\rm nc} \nabla \cdot (\mathbf{U}) = 0. \tag{49}$$

Rearranging the last equation yields

$$\frac{d\alpha_{\rm nc}}{dt} = -\alpha_{\rm nc} \nabla \cdot \mathbf{U}.\tag{50}$$

Looking at the time rate of change of the sum of volume fractions, it follows that

$$\frac{d\alpha_{l}}{dt} + \frac{d\alpha_{v}}{dt} + \frac{d\alpha_{nc}}{dt} = 0,$$

$$\frac{d\alpha_{l}}{dt} = -\frac{d\alpha_{v}}{dt} - \frac{d\alpha_{nc}}{dt}.$$
(51)

Substituting Eqn. 50 into Eqn. 51 yields

$$\frac{d\alpha_{\rm l}}{dt} = -\frac{d\alpha_{\rm v}}{dt} + \alpha_{\rm nc} \nabla \cdot \mathbf{U}.$$
 (52)

Substituting Eqn. 52 and Eqn. 43 into Eqn. 46 yields the following, with intermediate rearrangement steps shown to aid the reader in following along.

$$\frac{d\alpha_{\rm v}}{dt} = \alpha_{\rm l} 4n_{0} \pi R^{2} \frac{dR}{dt} + \left(-n_{0} \frac{4}{3} \pi R^{3} + n_{0} \frac{4}{3} \pi R^{3} \alpha_{\rm nc} \frac{(\rho_{\rm l} - \rho_{\rm v})}{\rho + \alpha_{\rm nc} (\rho_{\rm l} - \rho_{\rm nc})}\right) \frac{d\alpha_{\rm v}}{dt},$$

$$\alpha_{\rm l} 4n_{0} \pi R^{2} \frac{dR}{dt} = \left(1 + n_{0} \frac{4}{3} \pi R^{3} + n_{0} \frac{4}{3} \pi R^{3} \alpha_{\rm nc} \frac{(\rho_{\rm v} - \rho_{\rm l})}{\rho + \alpha_{\rm nc} (\rho_{\rm l} - \rho_{\rm nc})}\right) \frac{d\alpha_{\rm v}}{dt},$$

$$\frac{d\alpha_{\rm v}}{dt} = \frac{\alpha_{\rm l} 4n_{0} \pi R^{2} \frac{dR}{dt}}{1 + n_{0} \frac{4}{3} \pi R^{3} + n_{0} \frac{4}{3} \pi R^{3} \alpha_{\rm nc} \frac{(\rho_{\rm v} - \rho_{\rm l})}{\rho + \alpha_{\rm nc} (\rho_{\rm l} - \rho_{\rm nc})}},$$

$$\frac{d\alpha_{\rm v}}{dt} = \frac{\alpha_{\rm l} 4n_{0} \pi R^{2} \frac{dR}{dt} (\rho + \alpha_{\rm nc} (\rho_{\rm l} - \rho_{\rm nc}))}{\rho + \alpha_{\rm nc} (\rho_{\rm l} - \rho_{\rm nc}) + n_{0} \frac{4}{3} \pi R^{3} (\rho + \alpha_{\rm nc} (\rho_{\rm l} - \rho_{\rm nc}))}{n_{\rm l} 4n_{0} \pi R^{2} \frac{dR}{dt} (\rho + \alpha_{\rm nc} (\rho_{\rm l} - \rho_{\rm nc}))}{n_{\rm l} 4n_{0} \pi R^{2} \frac{dR}{dt} (\rho + \alpha_{\rm nc} (\rho_{\rm l} - \rho_{\rm nc}))},$$

$$\frac{d\alpha_{\rm v}}{dt} = \frac{\alpha_{\rm l} 4n_{0} \pi R^{2} \frac{dR}{dt} (\rho + \alpha_{\rm nc} (\rho_{\rm l} - \rho_{\rm nc}))}{\rho + \alpha_{\rm nc} (\rho_{\rm l} - \rho_{\rm nc}) + n_{0} \frac{4}{3} \pi R^{3} (\rho + \alpha_{\rm nc} (\rho_{\rm l} - \rho_{\rm nc}))},$$

$$\frac{d\alpha_{\rm v}}{dt} = \frac{\alpha_{\rm l} 4n_{0} \pi R^{2} \frac{dR}{dt} (\rho + \alpha_{\rm nc} (\rho_{\rm l} - \rho_{\rm nc}))}{\rho + \alpha_{\rm nc} (\rho_{\rm l} - \rho_{\rm nc}) + n_{0} \frac{4}{3} \pi R^{3} (\rho + \alpha_{\rm nc} (\rho_{\rm v} - \rho_{\rm nc}))},$$

$$\frac{d\alpha_{\rm v}}{dt} = \frac{\alpha_{\rm l} 4n_{0} \pi R^{2} \frac{dR}{dt}}{1 + n_{0} \frac{4}{3} \pi R^{3} (\rho + \alpha_{\rm nc} (\rho_{\rm v} - \rho_{\rm nc}))},$$

$$\frac{d\alpha_{\rm v}}{dt} = \frac{\alpha_{\rm l} 4n_{0} \pi R^{2} \frac{dR}{dt}}{1 + n_{0} \frac{4}{3} \pi R^{3} (\rho + \alpha_{\rm nc} (\rho_{\rm v} - \rho_{\rm nc}))}{\rho + \alpha_{\rm nc} (\rho_{\rm l} - \rho_{\rm nc})}.$$
(53)

Equation 53 is the evaporation term. For the condensation term, the derivation is similar to the derivation above. Implementing

$$\alpha_{\rm l} = \frac{3\alpha_{\rm v}}{4\pi n_0 R^3},\tag{54}$$

as a rewritten form of Eqn. 45 and again using the definition of total derivative yields

$$\frac{d\alpha_1}{dt} = -\frac{3\alpha_v \frac{dR}{dt}}{\frac{4}{3}\pi n_0 R^4} + \frac{3}{4\pi n_0 R^3} \frac{d\alpha_v}{dt}.$$
 (55)

By substituting Eqn. 52 and Eqn. 43 into Eqn. 55, a term for condensation rate can be obtained, as demonstrated below with all the intermediate rearrangement steps shown as

$$-\frac{d\alpha_{v}}{dt} + \alpha_{nc} \frac{(\rho_{l} - \rho_{v})}{\rho + \alpha_{nc} (\rho_{l} - \rho_{nc})} \frac{d\alpha_{v}}{dt} = -\frac{3\alpha_{v} \frac{dR}{dt}}{\frac{4}{\pi} n_{0} R^{4}} + \frac{3}{4\pi n_{0} R^{3}} \frac{d\alpha_{v}}{dt},$$

$$\left(-1 + \alpha_{nc} \frac{(\rho_{l} - \rho_{v})}{\rho + \alpha_{nc} (\rho_{l} - \rho_{nc})} - \frac{3}{4n_{0}\pi R^{3}}\right) \frac{d\alpha_{v}}{dt} = -\frac{3\alpha_{v} \frac{dR}{dt}}{\frac{4}{\pi} n_{0} R^{4}},$$

$$\frac{d\alpha_{v}}{dt} = \frac{-3\alpha_{v} \frac{dR}{dt}}{\left(-1 + \alpha_{nc} \frac{(\rho_{l} - \rho_{v})}{\rho + \alpha_{nc} (\rho_{l} - \rho_{nc})} - \frac{3}{4n_{0}\pi R^{3}}\right) \frac{4}{3}\pi n_{0} R^{4}},$$

$$\frac{d\alpha_{v}}{dt} = \frac{-3\alpha_{v} \frac{dR}{dt} \left(\rho + \alpha_{nc} \left(\rho_{l} - \rho_{nc}\right)\right)}{\left(-(\rho + \alpha_{nc} (\rho_{l} - \rho_{nc})) + \alpha_{nc} (\rho_{l} - \rho_{v}) - \frac{3}{4n_{0}\pi R^{3}} \left(\rho + \alpha_{nc} (\rho_{l} - \rho_{nc})\right)\right) \frac{4}{3}\pi n_{0} R^{4}},$$

$$\frac{d\alpha_{v}}{dt} = \frac{-3\alpha_{v} \frac{dR}{dt} \left(\rho + \alpha_{nc} (\rho_{l} - \rho_{nc})\right)}{\left(-\rho - \alpha_{nc} \rho_{l} + \alpha_{nc} \rho_{l} - \alpha_{nc} \rho_{v} - \frac{3}{4n_{0}\pi R^{3}} \left(\rho + \alpha_{nc} (\rho_{l} - \rho_{nc})\right)\right) \frac{4}{3}\pi n_{0} R^{4}},$$

$$\frac{d\alpha_{v}}{dt} = \frac{-3\alpha_{v} \frac{dR}{dt} \left(\rho + \alpha_{nc} (\rho_{l} - \rho_{nc})\right)}{\left(-\rho + \alpha_{nc} (\rho_{nc} - \rho_{v}) - \frac{3}{4n_{0}\pi R^{3}} \left(\rho + \alpha_{nc} (\rho_{l} - \rho_{nc})\right)\right) \frac{4}{3}\pi n_{0} R^{4}},$$

$$\frac{d\alpha_{v}}{dt} = \frac{-3\alpha_{v} \frac{dR}{dt}}{\left(\frac{-\rho + \alpha_{nc} (\rho_{nc} - \rho_{v})}{\rho + \alpha_{nc} (\rho_{l} - \rho_{nc})} - \frac{3}{4n_{0}\pi R^{3}}\right) \frac{4}{3}\pi n_{0} R^{4}},$$

$$\frac{d\alpha_{v}}{dt} = \frac{3\alpha_{v} \frac{dR}{dt}}{\left(\frac{-\rho + \alpha_{nc} (\rho_{nc} - \rho_{v})}{\rho + \alpha_{nc} (\rho_{l} - \rho_{nc})} - \frac{3}{4n_{0}\pi R^{3}}\right) \frac{4}{3}\pi n_{0} R^{4}},$$

$$\frac{d\alpha_{v}}{dt} = \frac{3\alpha_{v} \frac{dR}{dt}}{\left(\frac{-\rho + \alpha_{nc} (\rho_{nc} - \rho_{v})}{\rho + \alpha_{nc} (\rho_{l} - \rho_{nc})} - \frac{3}{4n_{0}\pi R^{3}}\right) \frac{4}{3}\pi n_{0} R^{4}},$$

$$\frac{d\alpha_{v}}{dt} = \frac{3\alpha_{v} \frac{dR}{dt}}{\left(\frac{-\rho + \alpha_{nc} (\rho_{nc} - \rho_{v})}{\rho + \alpha_{nc} (\rho_{l} - \rho_{nc})} - \frac{3}{4n_{0}\pi R^{3}}\right) \frac{4}{3}\pi n_{0} R^{4}},$$

$$\frac{d\alpha_{v}}{dt} = \frac{3\alpha_{v} \frac{dR}{dt}}{\left(\frac{-\rho + \alpha_{nc} (\rho_{nc} - \rho_{v})}{\rho + \alpha_{nc} (\rho_{l} - \rho_{nc})} - \frac{3}{4n_{0}\pi R^{3}}\right) \frac{4}{3}\pi n_{0} R^{4}},$$

The terms for condensation and evaporation can be summarised as

$$\frac{d\alpha_{\rm v}}{dt} = \begin{cases}
\frac{3\alpha_{\rm v}\frac{dR}{dt}}{\left(\frac{\rho + \alpha_{\rm nc}(\rho_{\rm v} - \rho_{\rm nc})}{\rho + \alpha_{\rm nc}(\rho_{\rm l} - \rho_{\rm nc})}\right)\frac{4}{3}\pi n_0 R^4 + R} & \text{if } p \ge p_{\rm sat} \\
\frac{\alpha_1 4 n_0 \pi R^2 \frac{dR}{dt}}{1 + n_0 \frac{4}{3}\pi R^3 \left(\frac{\rho + \alpha_{\rm nc}(\rho_{\rm v} - \rho_{\rm nc})}{\rho + \alpha_{\rm nc}(\rho_{\rm l} - \rho_{\rm nc})}\right)} & \text{if } p < p_{\rm sat}.
\end{cases}$$
(57)

References

- [1] Z. He, H. Zhou, L. Duan, M. Xu, Z. Chen, and T. Cao, "Effects of nozzle geometries and needle lift on steadier string cavitation and larger spray angle in common rail diesel injector," INTERNATIONAL JOURNAL OF ENGINE RESEARCH, vol. 22, no. 8, pp. 2673–2688, AUG 2021. [Online]. Available: https://doi.org/10.1177/1468087420936490
- [2] H. Ma, T. Zhang, Q. An, Y. Tao, and Y. Xu, "Visualization experiment and numerical analysis of cavitation flow characteristics in diesel fuel injector control valve with different structure design," JOURNAL OF THERMAL SCIENCE, vol. 30, no. 1, pp. 76–87, JAN 2021. [Online]. Available: https://doi.org/10.1007/s11630-020-1301-7
- [3] T. Cao, Z. He, H. Zhou, W. Guan, L. Zhang, and Q. Wang, "Experimental study on the effect of vortex cavitation in scaled-up diesel injector nozzles and spray characteristics," EXPERIMENTAL THERMAL AND FLUID SCIENCE, vol. 113, MAY 1 2020. [Online]. Available: https://doi.org/10.1016/j.expthermflusci.2019.110016
- [4] W. Guan, Z. He, L. Zhang, A. I. El-Seesy, L. Wen, Q. Zhang, and L. Yang, "Effect of asymmetric structural characteristics of multi-hole marine diesel injectors on internal cavitation patterns and flow characteristics: A numerical study," FUEL, vol. 283, JAN 1 2021. [Online]. Available: https://doi.org/10.1016/j.fuel.2020.119324
- [5] M. Cristofaro, W. Edelbauer, P. Koukouvinis, and M. Gavaises, "A numerical study on the effect of cavitation erosion in a diesel injector," APPLIED MATHEMATICAL MODELLING, vol. 78, pp. 200–216, FEB 2020. [Online]. Available: https://doi.org/10.1016/j.apm.2019.09.002
- [6] H. Chaves, M. Knapp, A. Kubitzek, F. Obermeier, and T. Schneider, "Experimental study of cavitation in the nozzle hole of diesel injectors using transparent nozzles," SAE Transactions, vol. 104, pp. 645–657, 1995. [Online]. Available: http://www.jstor.org/stable/44633242
- [7] R. Ravendran, "Cylinder lubrication of two-stroke diesel engines: Investigation of nozzle flow and spray formation using numerical simulation and experimental visualisation," Ph.D. dissertation, The Doctoral School of Engineering and Science, 2018. [Online]. Available: https://aauforlag.dk/produkt/phd-udgivelse/phd-rathesan-ravendran
- [8] M. Heinrich and R. Schwarze, "3d-coupling of volume-of-fluid and lagrangian particle tracking for spray atomization simulation in openfoam," SoftwareX, vol. 11, p. 100483, 2020. [Online]. Available: https://doi.org/10.1016/j.softx.2020.100483
- [9] W. Yuan and G. H. Schnerr, "Numerical simulation of two-phase flow in injection nozzles: Interaction of cavitation and external jet formation," *Journal of Fluids Engineering, Transactions of the ASME*, vol. 125, no. 6, pp. 963–969, 2003. [Online]. Available: https://doi.org/10.1115/1.1625687
- [10] F. Giussani, F. Piscaglia, G. Saez-Mischlich, and J. Hèlie, "A three-phase VOF solver for the simulation of in-nozzle cavitation effects on liquid atomization," *Journal of Computational Physics*, vol. 406, p. 109068, 2020. [Online]. Available: https://doi.org/10.1016/j.jcp.2019.109068
- [11] B. C. Dueholm, "Implementation of a vof solver with phase change for the simulation of internal cavitation and droplet breakup in injectors," in Proceedings of CFD with OpenSource Software, 2021, Edited by Nilsson. H. [Online]. Available: http://dx.doi.org/10.17196/OS_CFD#YEAR_2021
- [12] H. Jasak, "Error analysis and estimation for the finite volume method with applications to fluid flows," Ph.D. dissertation, Imperial College London, 01 1996. [Online]. Available: https://spiral.imperial.ac.uk/handle/10044/1/8335
- [13] G. H. Schnerr and J. Sauer, "Physical and Numerical Modeling of Unsteady Cavitation Dynamics," 4th International Conference on Multiphase Flow, no. June, pp. 1–12, 2001. [Online]. Available: https://www.researchgate.net/publication/296196752_Physical_and_Numerical_Modeling_of_Unsteady_Cavitation_Dynamics
- [14] L. R. O. F.R.S., "Viii. on the pressure developed in a liquid during the collapse of a spherical cavity," The London, Edinburgh, and Dublin Philosophical Magazine and Journal of Science, vol. 34, no. 200, pp. 94–98, 1917. [Online]. Available: https://doi.org/10.1080/14786440808635681
- [15] A. Ahmed, "LES of atomization and cavitation for fuel injectors," no. August, 2019. [Online]. Available: http://www.theses.fr/2019NORMR048/document
- [16] A. Sou, B. Biçer, and A. Tomiyama, "Numerical simulation of incipient cavitation flow in a nozzle of fuel injector," Computers & Fluids, vol. 103, pp. 42–48, 2014. [Online]. Available: https://doi.org/10.1016/j.compfluid.2014.07.011
- [17] B. Biçer and A. Sou, "Application of the improved cavitation model to turbulent cavitating flow in fuel injector nozzle," Applied Mathematical Modelling, vol. 40, no. 7, pp. 4712–4726, 2016. [Online]. Available: https://doi.org/10.1016/j.apm.2015.11.049
- [18] N. Franck and F. Ducros, "Subgrid-scale stress modelling based on the square of the velocity gradient tensor," Flow Turbulence and Combustion, vol. 62, pp. 183–200, 09 1999. [Online]. Available: https://doi.org/10.1023/A: 1009995426001